

● *Original Contribution*

POST-PROCEDURE EVALUATION OF MICROWAVE ABLATIONS OF HEPATOCELLULAR CARCINOMAS USING ELECTRODE DISPLACEMENT ELASTOGRAPHY

WENJUN YANG,^{*} TIMOTHY J. ZIEMLEWICZ,[†] TOMY VARGHESE,^{*‡} MARCI L. ALEXANDER,[†]
NICHOLAS RUBERT,^{*} ATUL N. INGLE,[‡] MEGHAN G. LUBNER,[†] JAMES L. HINSHAW,[†] SHANE A. WELLS,[†]
FRED T. LEE, JR.,[†] and JAMES A. ZAGZEBSKI^{*}

^{*}Department of Medical Physics, University of Wisconsin School of Medicine and Public Health, University of Wisconsin–Madison, Madison, Wisconsin, USA; [†]Department of Radiology, University of Wisconsin School of Medicine and Public Health, University of Wisconsin–Madison, Madison, Wisconsin, USA; and [‡]Department of Electrical and Computer Engineering, University of Wisconsin–Madison, Madison, Wisconsin, USA

(Received 21 December 2015; revised 2 May 2016; in final form 13 July 2016)

Abstract—Microwave ablation has been used clinically as an alternative to surgical resection. However, lack of real-time imaging to assess treated regions may compromise treatment outcomes. We previously introduced electrode displacement elastography (EDE) for strain imaging and verified its feasibility *in vivo* on porcine animal models. In this study, we evaluated EDE on 44 patients diagnosed with hepatocellular carcinoma, treated using microwave ablation. The ablated region was identified on EDE images for 40 of the 44 patients. Ablation areas averaged $13.38 \pm 4.99 \text{ cm}^2$ on EDE, compared with $7.61 \pm 3.21 \text{ cm}^2$ on B-mode imaging. Contrast and contrast-to-noise ratios obtained with EDE were 232% and 98%, respectively, significantly higher than values measured on B-mode images ($p < 0.001$). This study indicates that EDE is feasible in patients and provides improved visualization of the ablation zone compared with B-mode ultrasound. (E-mail: tvarghese@wisc.edu) © 2016 World Federation for Ultrasound in Medicine & Biology.

Key Words: Ablation, Elastography, Elasticity imaging, Microwave ablation, Hepatocellular carcinoma, Strain imaging.

INTRODUCTION

Hepatocellular carcinoma (HCC) is the sixth most common cancer and third leading cause of cancer-related mortality worldwide (Lencioni and Crocetti 2012). Surgical resection of liver tissue was the standard procedure for the cure of HCC, although there are critical constraints for its widespread use. Specific criteria have to be met for successful surgical resection: (i) The cancer is limited to a single liver lobe; (ii) liver function is well preserved; and (iii) the patient has neither abnormal bilirubin nor portal hypertension (Lencioni and Crocetti 2007). However, cirrhosis commonly occurs with HCC, and only up to 5% of cirrhotic patients with HCC fit the constraints described above for liver resection (Lencioni and Crocetti

2007). Therefore, only 9% of patients with HCC are suitable candidates for surgical resection (Liang and Wang 2007). With the development of minimally invasive treatments such as percutaneous radiofrequency ablation (RFA) and microwave ablation (MWA), thermal ablation has been adopted as the primary treatment option for HCC, especially for early-stage interventions (tumor size $< 3 \text{ cm}$) (Lencioni and Crocetti 2012; Shiina et al. 2012). Existing clinical studies have indicated that treatment outcomes with ablation procedures are superior or at least equivalent to surgical resection or ethanol injection for these early-stage HCC tumors (Lencioni and Crocetti 2007, 2012; Liang and Wang 2007; Lu et al. 2005; Maluccio and Covey 2012; Shiina et al. 2012).

Microwave ablation, introduced as an ablation technique initially in Japan (Murakami et al. 1995), has now been increasingly applied worldwide (Liang and Wang 2007; Lu et al. 2005; Maluccio and Covey 2012; Qian et al. 2012; Shibata et al. 2002; Swan et al. 2013).

Address correspondence to: Tomy Varghese, Department of Medical Physics, University of Wisconsin School of Medicine and Public Health, University of Wisconsin–Madison, Madison, WI 53706, USA. E-mail: tvarghese@wisc.edu

Instead of generating the thermal dose by incorporating the patient as part of a closed-loop circuit as in RFA, MWA emits microwave energy to agitate water molecules, causing coagulation necrosis with a local impact. Thus, MWA delivers consistently higher intra-tumor temperatures, with reduced impact from blood flow in large vessels, enables faster ablation times and provides an improved convection profile (Lencioni and Crocetti 2012; Liang and Wang 2007; Qian et al. 2012). Multiple probes can be applied simultaneously to create larger tumor ablation volumes (Harari et al. 2015). MWA therefore has several advantages over RFA including increased power, increased volume of direct heating, ablation consistency in different tissue types and no requirement for ground pads (Lubner et al. 2013; Wells et al. 2015; Ziemlewicz et al. 2016). With these technological advantages, MWA has been increasingly cited as the more commonly used percutaneous ablation method (Wells et al. 2015; Ziemlewicz et al. 2015). Some investigators have reported that MWA does not result in an obvious improvement over RFA in treatment outcomes (Lu et al. 2005; Qian et al. 2012; Shibata et al. 2002); however, these studies used previous-generation microwave technology. In evaluations of current-generation technology, MWA has resulted in a significantly lower rate of local tumor progression than RFA (Potretzke et al. 2016). The modality limitation might also be compensated by other treatment methods such as trans-arterial chemoembolization (TACE) to limit the blood supply from the hepatic artery to reduce the heat sink effect of large vessels (Liang and Wang 2007; Maluccio and Covey 2012). One recent study reported that MWA could lead to satisfactory outcomes even for tumors larger than 3 cm, which was previously considered to be the maximum suitable size for thermal ablation procedures (Ziemlewicz et al. 2015).

Ultrasound elastography has been considered as an alternative for ablation monitoring because the stiffness contrast between an ablated region and surrounding tissue is high (Bharat et al. 2005, 2008b; Fahey et al. 2008; Kolokythas et al. 2008; Mariani et al. 2014; Righetti et al. 1999; Rubert et al. 2010; Varghese et al. 2002, 2003a; Zhang et al. 2008; Zhou et al. 2014) and is not significantly affected by the presence of gas bubbles (Varghese et al. 2004). Conventional, quasi-static ultrasound elastography is dependent on either externally applied compression (Ophir et al. 1991) or internal physiologic deformations (Shi and Varghese 2007; Varghese and Shi 2004; Varghese et al. 2003b) to produce displacements for estimating local tissue strain. The need for an external compressor would restrict the use of ultrasound elastography because it is cumbersome and generally cannot produce tissue displacements at sufficient depth. Acoustic radiation force impulse

(ARFI) (Bing et al. 2011; Fahey et al. 2008; Hoyt et al. 2008; Mariani et al. 2014; Nightingale et al. 2001; Sarvazyan et al. 1998) may be more suited for this task, but ARFI is limited by the small tissue displacements that can be generated (around 0.01 mm) and a relatively shallow imaging depth of around 8 cm. Beyond this depth, the acoustic radiation force generated is too small to deform tissue because of attenuation of the signal (Deng et al. 2015; Zhao et al. 2011). The resulting data are also very sensitive to physiologic motion such as cardiac pulsation and respiratory artifacts.

We previously introduced a novel, quasi-static ultrasound elastography technique, referred to as *electrode displacement elastography* (EDE) (Bharat et al. 2008b; Rubert et al. 2010; Varghese et al. 2002), designed specifically for monitoring percutaneous ablation procedures. Here the local tissue deformation for elastography is induced by manual perturbation of the ablation antenna (Varghese et al. 2002). In this article, we investigated the feasibility of EDE in a pilot study on 44 patients diagnosed with HCC and treated with MWA. The delineation of the ablated region on EDE images was compared with ablated region contours taken from conventional B-mode images. The two modalities were compared with respect to estimated ablation zone area and detectability using contrast and contrast-to-noise ratio (CNR) features.

METHODS

Patients and MWA system

Forty-four patients who underwent MWA for their HCC tumors were involved in this study. Informed consent to participate in this study was obtained before the ablation procedure under a protocol approved by the institutional review board at the University of Wisconsin–Madison. Patients received MWA treatments under general anesthesia. Ultrasound radiofrequency data for EDE were acquired after antenna insertion, before onset of ablation and immediately after the ablation procedure before the ablation antenna was removed from the insertion site. EDE images that exhibited clearly distinguishable ablation regions were obtained for 40 of the 44 patients. Four patients were excluded from analysis because the ablation zone could not be clearly delineated because of insufficient compression or excessive signal decorrelation artifacts.

Microwave ablation was performed with a Neuwave Medical Certus 140 (Madison, WI, USA) operating at 2.45 GHz. Ablation duration and power were adjusted for each patient depending on tumor size and location, with typical values of 5 min and 65 W, respectively. The MWA antenna was inserted under conventional ultrasound B-mode imaging guidance in a computed

tomography (CT) imaging suite. In several patients, multiple MWA antennas (maximum of three, typically two) were inserted at the same ablation site. MWA antenna position and placement within the ablation region were also confirmed using CT scans before the ablation procedure in cases where ultrasound B-mode imaging was not definitive. B-mode and EDE strain images were obtained after completion of the active ablation procedure but before complete dissipation of the gas bubbles to evaluate the post-treatment appearance.

EDE techniques and strain image processing

The mechanical stimulus for EDE was induced by a physician who manually perturbed the ablation antenna. A small displacement (typically around 1 mm) was applied to the ablated region through the perturbation. No side effects, such as additional bleeding and patient discomfort, were noted as a result of the EDE procedure.

Loops of ultrasound radiofrequency data were recorded during the perturbation of the antenna. Data were acquired using a Siemens ACUSON S2000 system equipped with a curvilinear array transducer (6 C1 HD) operating at a 4 MHz center frequency. Two frames of radiofrequency data were selected as “pre” and “post” deformation frames after review of the entire loop of images generated from the radiofrequency data. These data were then processed to estimate local tissue displacements. We selected frames such that the correlation coefficient between kernels did not drop below 0.75 at all depths to ensure that local displacements estimated are accurate (Chen and Varghese 2009). A 2-D cross-correlation-based tracking algorithm (Chen *et al.* 2009) was applied, with the cross-correlation kernel dimensions $3.5 \text{ wavelengths} \times 7 \text{ A-lines}$. Assuming a sound speed of 1540 m/s, and at a depth of 8 cm, the physical dimensions of the kernel were $1.35 \times 3.29 \text{ mm}$ along the axial and lateral directions, respectively. The kernel dimensions used are larger than those applied in breast elastography, where high-frequency linear array transducers are used and kernel sizes of $0.385 \text{ mm (axial)} \times 0.507 \text{ mm (lateral)}$ are applied (Xu *et al.* 2012). The larger kernel size was required in this study because of the increased attenuation at deeper imaging locations, reducing the echo data signal-to-noise ratio, lower center frequency and smaller deformations introduced with EDE. Adjacent cross-correlation kernels overlapped by 80% along the beam direction and one A-line in the lateral direction. Local displacement estimates were fit with a 15-point (3.78 mm) linear, least-squares fit, and the local strain values were computed as the gradient of the local displacements. EDE-based strain images were generated offline on an Intel Core 2 Duo computer, with the tracking algorithm implemented using MATLAB (The MathWorks, Natick, MA, USA).

To account for the fan-shaped geometry of data acquired using the curvilinear transducer, scan conversion was applied after displacement and strain estimations along the direction of the A-lines. A bi-linear interpolation was then applied to the strain values to calculate pixel values at scan converted positions on a rectangular grid.

Evaluation metrics for EDE versus conventional B-mode imaging

Area of the ablation region. Ablated zones are recognized in EDE because they exhibit lower strain than surrounding, untreated tissue. The estimated area of the ablation region was used as a feature to compare the 2-D distribution of the low-strain zone on EDE and the hyper-echoic region on B-mode images. The ablation region was segmented manually on both sets of images. The area of the ablation region, S , was calculated using

$$S = \Delta \times N \quad (1)$$

where Δ is the image pixel size, and N is the number of pixels inside the segmented region.

Ablation region contrast. The contrast of the ablation region is defined as

$$C = \frac{|I_o - I_b|}{I_o + I_b} \quad (2)$$

where C represents the contrast, I_o is the mean image pixel value of a rectangular region of interest (ROI) positioned within the ablated region and I_b is the mean pixel value of a similar-sized rectangular ROI adjacent to the ablated region.

For EDE, the ROI of the ablated region was defined within the dark ellipse (Fig. 1, for example), which is the region with increased tissue stiffness. The background ROI was defined outside the bright halo around the ablated region. The upper limit of the strain values on the EDE images was set to a maximum of 0.025 or 2.5%, which was the approximate upper limit of the strain value introduced by the small needle perturbation. For B-mode images, the ROI of the ablated region was defined within the bright gas bubble region, and the background ROI was selected from a region adjacent to the bubbles.

CNR of the ablation region. The CNR takes into consideration the noise level of the ablation region and background and is used to describe the detectability of the ablated region with the EDE strain image (Varghese and Ophir 1998). The CNR of the ablation region was calculated using

$$\text{CNR} = 20 \log_{10} \left(\frac{|I_o - I_b|}{\sqrt{\sigma_o^2 + \sigma_b^2}} \right) \quad (3)$$

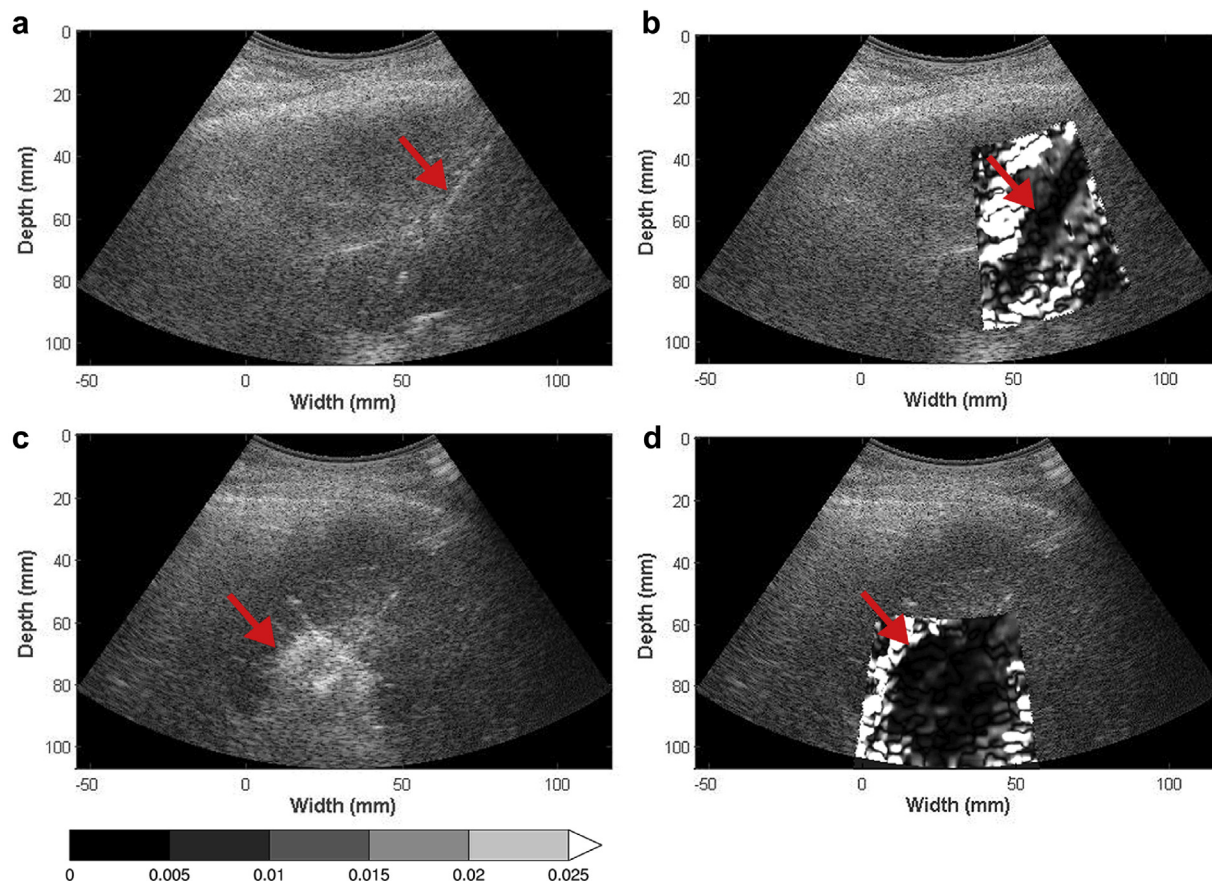


Fig. 1. Pre- and post-ablation regions depicted on electrode displacement elastography (EDE) strain and corresponding B-mode images for a patient diagnosed with a 2.0-cm hepatocellular carcinoma tumor. The targeted tumor regions on the B-mode (a) and EDE (b) images are in the top row, whereas the ablated regions on the B-mode (c) and corresponding EDE strain (d) images are in the bottom row. The ablation needle on the pre-treatment image (a) is identified by the echogenic line on the B-mode image. EDE strain images were generated with a $3.5 \text{ wavelength} \times 7 \text{ A-line}$ cross-correlation kernel. The upper limit of the strain value was 2.5%, and all values beyond were saturated as indicated by the color bar. The red arrow points to the MWA antenna in (a) and (b), and the ablated region in (c) and (d) respectively.

where σ_o^2 and σ_b^2 represent the variance of the strain estimates within the ROI defined in the ablation region and background, respectively.

Measurement methods

Visualization and comparison of ablated regions on EDE strain and B-mode images in this study were not designed as a blinded study. A single observer with experience in *ex vivo* and *in vivo* MWA experiments delineated the ablated region area and selected the ROI for estimation of the contrast and CNR for both B-mode and EDE strain images. B-mode images were analyzed before EDE strain images.

Statistical analysis

The area, contrast and CNR of the ablated region on EDE strain and B-mode images were compared pairwise for each patient studied. These were presented in the

form of a scatter plot. Box-and-whisker plots were then used to perform a clustered comparison for the 40 patients, with the median value being the center bar within the box; the first and second quartile values the upper and lower borders of the box; and the 10th and 90th percentile values the top and bottom bars. The p values of the hypothesis that the values generated with EDE are greater than those with B-mode images were calculated and are represented by the number of asterisks above the box-and-whisker plots.

RESULTS

The high modulus contrast between the ablated region and the surrounding healthy tissue leads to a “saturated halo” appearance around the ablation zone on the EDE strain image, as illustrated in Figure 1. Previous studies on tissue-mimicking phantoms and *in vivo* porcine models revealed that the ablation zone on EDE matches histopathologic ablation contours well in terms

of target area and dimensions (Bharat *et al.* 2008b; Jiang *et al.* 2010; Rubert *et al.* 2010).

Figure 1 presents both the pre- and post-ablation EDE strain and B-mode images for a patient with a 2-cm HCC diagnosed using pre-ablation magnetic resonance imaging. The liver was cirrhotic, and the patient had not undergone any prior treatment for this tumor. HCC tumors are softer than normal liver tissue and, thus, would be significantly softer than cirrhotic liver tissue (DeWall *et al.* 2012a). Note the clear visualization of two MWA antennas in the B-mode image obtained before the ablation, as two antennas were placed for this patient. The pre-ablation EDE strain image indicates the presence of a small stiffer region surrounding the ablation needle because of the cryo-lock feature used to prevent needle movement after antenna placement and an area of increased decorrelation at the location of the second antenna. MWA ablation was performed for 5 min at a 65-W power level in this patient. The post-ablation EDE image indicates the ablated region is an ellipsoidal region of increased stiffness (Bharat *et al.* 2005; Kiss *et al.* 2009) that incorporates the ablation region produced from both antennas. The needle track in the post-ablation images indicates the antenna that was perturbed to generate the EDE strain images in Figures 1–3.

Ablation zones viewed on EDE were compared with those seen on conventional ultrasound B-mode images in terms of ablation region area, contrast and CNR. The maximum dimension of the ablated region is outlined in Figures 2 and 3, for both EDE and B-mode images, corresponding to the length of the major axis of the low-strain region and the gas bubble cloud formed immediately after the ablation procedure. Note in Figure 2 that the locations of the segment with the largest dimension in both images do not coincide, and this was the case with most of the ablations. Therefore, a more representative

metric such as the ablation area and strain contrast was used in our analysis. Also observe in Figure 3 that the gas bubble region does not coincide with the ablated region.

Figures 4–7 summarize the different features used to compare the performance of EDE-based strain imaging versus conventional B-mode imaging for evaluating the ablation zone after completion of the procedure. Scatter plots provide measurements from all 40 patients, with the *horizontal lines* denoting the means of the EDE and B-mode measurements, respectively. For the box-and-whisker plots, the *dashed long horizontal bar* in each data set represents the median value, with the first and third quartiles defined by the box, whereas the error bar represents the 10% and 90% values of the distribution of the measured feature values.

Ablation region area on EDE and B mode images

In Figure 4(a) are scatter plots comparing ablation areas estimated with EDE with areas of the hyperechoic regions on B-mode images. Each vertical pair of *filled circles and triangles* denotes values for EDE strain and B-mode, respectively, for the same patient. The average area of the ablation zone on EDE was $13.38 \pm 4.99 \text{ cm}^2$ (\pm standard deviation for all values). As a comparison, the average area on B-mode images for the same patient data set was $7.61 \pm 3.21 \text{ cm}^2$. A statistical comparison of the ablation area visualized on EDE strain with the area on B-mode imaging is illustrated in Figure 4(b).

Contrast of ablation region on EDE and B-mode

In a similar manner, the distribution of the contrast obtained for the 40 patients is illustrated in Figure 5(a). The mean value of the ablation zone contrast on EDE strain images was 0.73 ± 0.08 , whereas the mean value

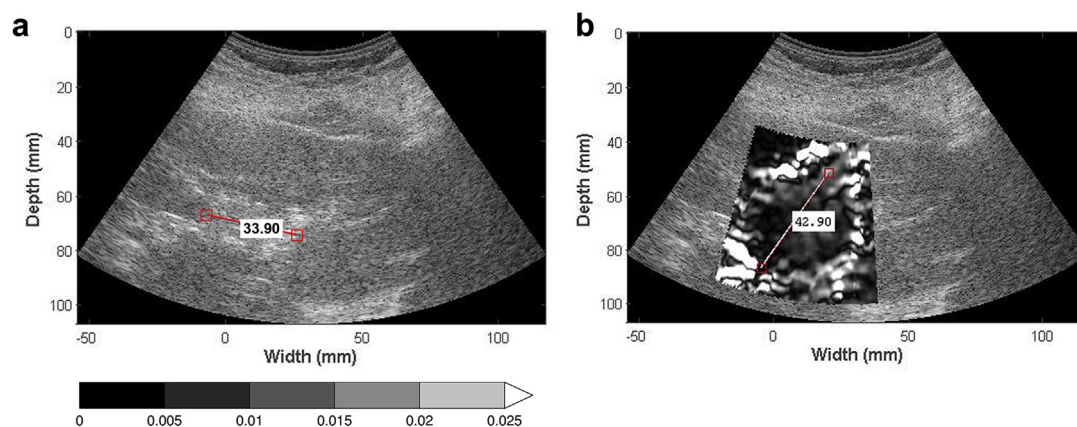


Fig. 2. Ablation region dimension measurements on electrode displacement elastography (EDE) and B-mode images. The maximum ablation region dimension on B-mode (a) and EDE strain (b) images was measured. The gas bubble cloud on B-mode images may be distorted, which results in measurement of the maximum dimension along different axes compared with the EDE strain image, as seen in (a) and (b).

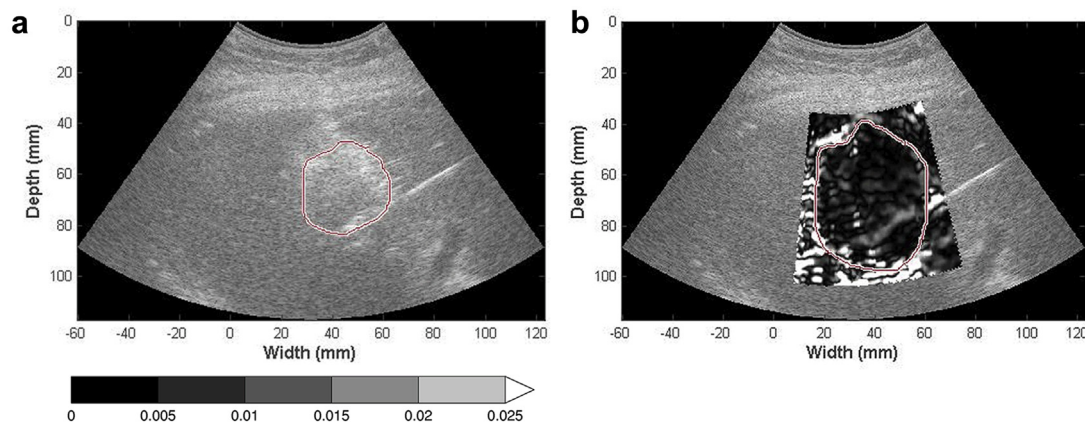


Fig. 3. Ablation area measurement on electrode displacement elastography (EDE) and B-mode images. The ablation region on B-mode (a) and EDE (b) images was segmented manually with the segmented area calculated using eqn (1). The gas bubble cloud depicted as the hyper-echoic region on B-mode images (a) tended to accumulate at variable locations.

of contrast on B-mode images for the same patient data set was 0.22 ± 0.08 , as indicated by the *horizontal lines* in Figure 5(a). The scatter plot for the contrast indicates a significant separation between the contrast estimated for EDE and the B-mode contrast of the ablated region. The distribution of contrast between the ablation area and background is illustrated in Figure 5(b). Strain imaging appears to provide a significant improvement in ablation region delineation based on the contrast ($p < 0.001$).

CNR of the ablated region on EDE and B-mode images

Finally, the CNR distribution for both EDE strain and B-mode imaging is illustrated in Figure 6(a). The average CNR of the ablation zone on EDE was 10.94 ± 2.45 dB, whereas the average CNR on B-mode images was 5.52 ± 3.37 dB. Observe that the CNR is always positive with EDE, whereas the CNRs obtained

with B-mode imaging indicate a few cases with extremely poor CNR leading to reduced detectability of the ablated region. The box-and-whisker plots for the CNR for EDE strain and B-mode imaging are provided in Figure 6(b).

Figure 7 is a 2-D scatter plot of contrast versus ablation area for each patient. Observe the separation between the B-mode estimates for the 40 patients from the EDE estimates, which exhibit a higher contrast and larger ablation areas.

DISCUSSION

Electrode displacement elastography was used on patients undergoing MWA therapy as a potential modality to define the post-procedure zone of ablation in this study. Strain images obtained using EDE had improved ablation region delineation compared with conventional

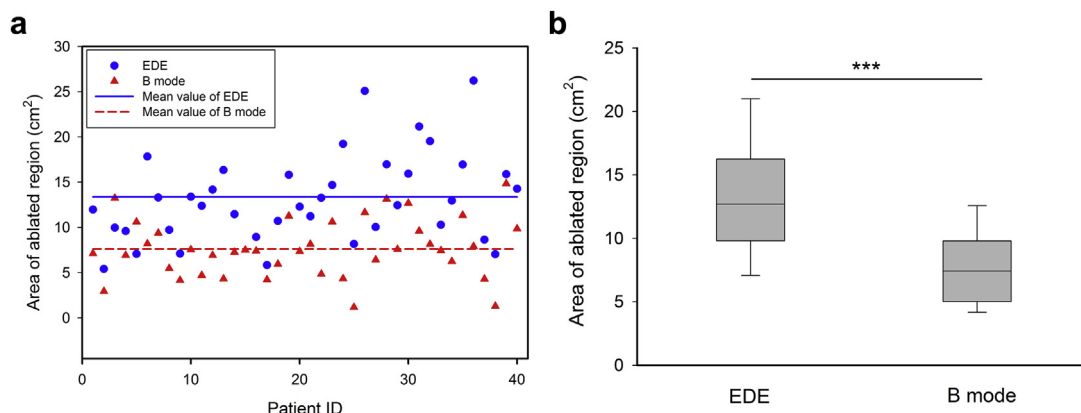


Fig. 4. Comparison of the ablation area measurements from B-mode (*triangles*) and electrode displacement elastography (EDE) strain (*circles*) images, using scatter (a) and box-and-whisker (b) plots. The mean value of the measurements is represented by the *horizontal line* in the scatter plot. For the box-and-whisker plot (b), the *dashed long horizontal bar* in each data sets denotes the median value. The p value was < 0.001 when comparing the mean values of EDE and corresponding B-mode images, denoted by the three asterisks.

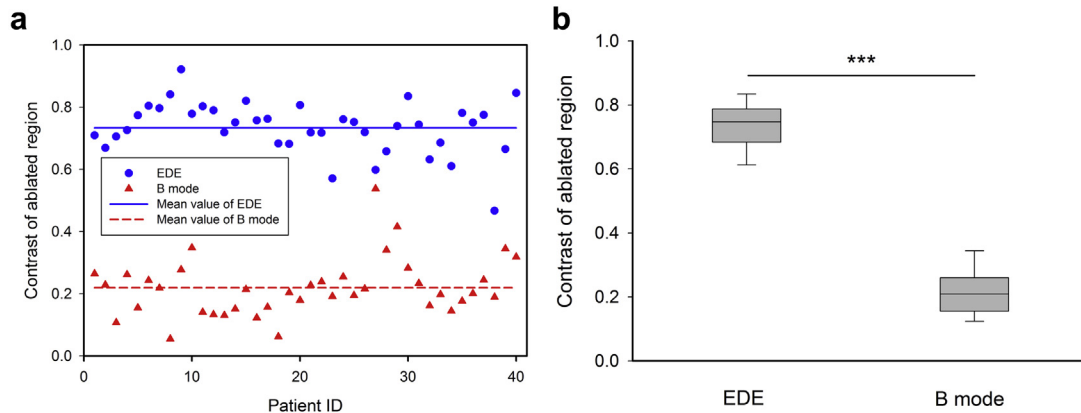


Fig. 5. Comparison of the ablation contrast measurements on B-mode (*triangles*) and electrode displacement elastography (EDE) strain (*circles*) images, using scatter (a) and box-and-whisker plots (b). The p value was < 0.001 when comparing the mean values of EDE and corresponding B-mode images, denoted by the three *asterisks*.

B-mode images in terms of ablation area, image contrast and CNR, as illustrated in [Figures 4–7](#). In addition, an approach that vibrates the ablation needle to generate and image shear waves, termed *electrode vibration elastography*, has also been developed ([Bharat and Varghese 2010](#); [DeWall and Varghese 2012](#); [DeWall et al. 2012b](#); [Ingle and Varghese 2014](#)).

In conjunction with EDE, ultrasound could become an effective modality for complete monitoring of the ablation zone during MWA treatments. Although conventional B-mode imaging is used routinely in the clinic for guidance of ablation antenna/electrode placement and for monitoring outgassing, it does not clearly define the ablation zone at the completion of the procedure ([Malone et al. 1994](#)). Currently the most common method used to monitor the ablation margin at the completion of the procedure is X-ray CT. Contrast CT, the current clinical standard for confirmation of the success of the procedure, provides ablation zone volume estimation and margin

definition. However, CT may not be available during the procedure in many centers. This may necessitate a repeated ablation procedure and re-insertion of an antenna in the liver if the ablation zone does not adequately cover the targeted tumor and tissue margins. Ultrasound EDE is non-ionizing and thus can be performed without radiation exposure of either the patient or physician. The 44 patients involved in this study included 10 females and 34 males, ranging in age from 33 to 83, as summarized in [Table 1](#).

It is important when treating with RFA to limit variations in thermal dose within the ablation volume and to avoid delivery of an incomplete dose to tumors, including those that are adjacent to large vessels ([Lencioni and Crocetti 2012](#)). This limits the application of RFA to smaller tumors and those away from large vessels (unless other precautions are taken). Large tumors and those near large vessels exhibit a decrease of up to 50% in terms of complete tumor necrosis ([Lencioni and Crocetti 2012](#)).

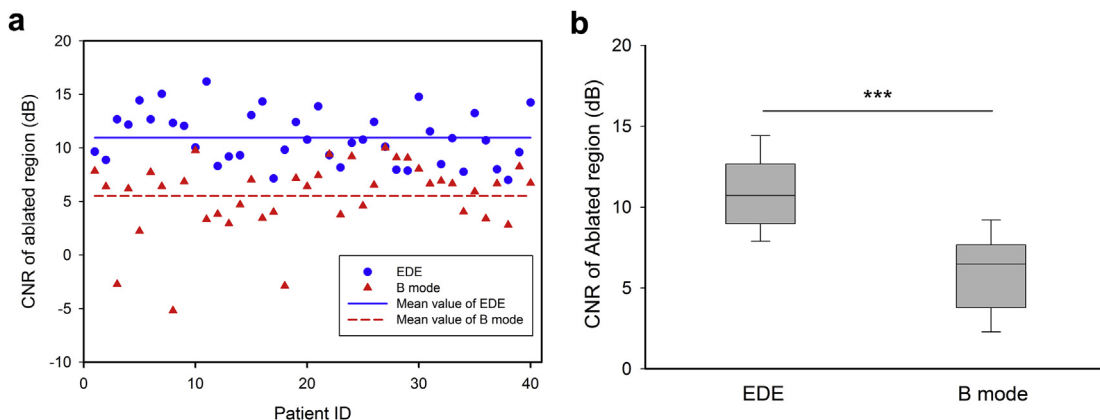


Fig. 6. Comparison of the contrast-to-noise ratio (CNR) measurements on B-mode (*triangles*) and electrode displacement elastography (EDE) strain (*circles*) images, using scatter (a) and box-and-whisker plots (b). The p value was < 0.001 when comparing the mean values of EDE and corresponding B-mode images, denoted by the three *asterisks*.

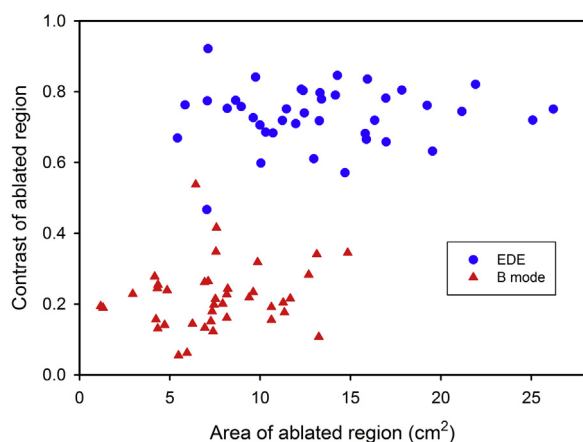


Fig. 7. Two-dimensional scatter plot illustrating ablation area versus contrast estimates for the ablated hepatocellular carcinoma tumors for B-mode (triangles) and electrode displacement elastography (EDE) strain (circle) images. Observe the clustering of the B-mode and EDE data sets.

An adequate ablation margin around the tumor region is a key factor in the success of percutaneous ablation treatments (Lencioni and Crocetti 2007, 2012; Maluccio and Covey 2012). Various studies suggest that the margin should extend between 0.5 and 1.0 cm into the tumor-free region (Lencioni and Crocetti 2007, 2012; Maluccio and Covey 2012). Thus, an effective thermal ablation margin monitoring method is crucial to guarantee a successful clinical outcome. Immediately after ablation therapy, a hyper-echoic area is observed on ultrasound B-mode images because of the out-gassing of water vapor, which resolves within about 10 min after the procedure. The ablated region with MWA is slightly hyper-echoic centrally and around the periphery and hypo-echoic elsewhere (Wells et al. 2015; Ziemlewicz et al. 2016). Contrast-enhanced ultrasound imaging has also been useful in delineating HCC tumors pre-ablation (Minami and Kudo 2011) and the coagulated region post-ablation (Clevert et al. 2012).

Even in cases where ablation area estimations on B-mode images were relatively close to those obtained on EDE strain images, estimates of ablated areas on

B-mode images were always smaller because of a shadowing effect, as illustrated in Figure 3. In Figure 3(b) the gas bubbles tended to accumulate toward the top of the ablation zone, and therefore, the lower boundary of the ablation zone was blurred because of the shadowing effect caused by increased attenuation from the gas bubbles. Thus, it was difficult to visualize the thermal dose distribution on the bottom half of the ablated region on B-mode images, and this increases the uncertainty of physicians in judging whether an adequate ablation margin has been applied uniformly around the ablation zone. On the other hand, as illustrated in Figure 3(a), the ablation zone could be clearly identified on EDE strain images. Thus, the thermal dose distribution along any direction can be easily observed.

On the basis of the estimated ablation areas, EDE strain images were not significantly affected by tumor depth, as outlined in Table 2. EDE provides delineation of the ablated region for treated HCC regions both at shallow depths and at deeper sites. This result is unlike that reported for elastographic imaging using acoustic radiation force, which is generally limited by ultrasonic attenuation to depths lower than 8 cm (Deng et al. 2015; Zhao et al. 2011).

The major limitation of this study was the lack of real-time EDE imaging feedback to the physicians. Image processing was performed offline on an Intel Core 2 desktop computer. The average processing time for each EDE strain image was approximately 1 min. To obtain real-time feedback, a higher-performance system or more efficient programming techniques would be necessary. This lack of real-time feedback also potentially affected the success rate of EDE strain imaging. We performed EDE on 44 patients and obtained successful strain imaging results in terms of distinguishable ablation zones on 40 of the 44 patients. The success rate was 90.9%, which would have been considerably improved by the immediate feedback that real-time imaging would have provided to the physician (Hall et al. 2003). Real-time feedback would allow physicians to more easily standardize the applied deformation using the ablation antenna. Several vendors currently do

Table 1. Statistics of patients with hepatocellular carcinoma reported in this study

Patient feature	Value
Age, y*	64.4 ± 9.3
Gender, M/F	34/10
Tumor size, cm*	2.2 ± 0.8
Cirrhosis, Y/N	37/7
Fatty liver, Y/N	1/43
Prior treatment, Y/N	10/34

F = female; M = male; N = no; Y = yes.

* Given as mean ± standard deviation.

Table 2. Details on HCC tumor depths and EDE imaging success for 44 patients

HCC depth, cm	No. of HCCs	EDE success	EDE success rate, %
<5	9	8/9	88.9
>5, <8	22	20/22	90.9
>8, <10	5	5/5	100
>10, <15	8	7/8	87.5
Total	44	40/44	90.9

EDE = electrode displacement elastography; HCC = hepatocellular carcinoma.

provide such feedback on their commercial elastography software, and this aspect can be easily addressed for this clinical application (Hall *et al.* 2003).

A second limitation of the study is the lack of ultrasound- or EDE-based volume information on the ablated region. We have previously reported that 3-D volume reconstruction of ablated regions using EDE can be achieved (Bharat *et al.* 2008a); however, a viable method of obtaining 3-D imaging information clinically in patients is essential. This can be done with either 2-D ultrasound arrays or more efficient scanning approaches (Ingle and Varghese 2014).

Side effects of EDE

The magnitude of the perturbation applied to the ablation antenna is within 1–2 mm. During the deformation of surrounding tissue and the ablated region, no relative slip between the surrounding tissue and ablation antenna was observed with EDE before or after the MWA procedure. There were no obvious side effects with EDE because the positioning of the ablation antenna was not affected after data acquisition. Because of the small range of displacements introduced by the antenna, the ablation procedure is not adversely affected (Varghese *et al.* 2002; Kolokythas *et al.* 2008; Varghese 2009).

CONCLUSIONS

In the study described here, we found that EDE is feasible during MWA procedures on HCC tumors regardless of tumor depth. EDE strain images provide improved ablation region delineation compared with conventional B-mode imaging. Further work needs to be performed to assess the accuracy of the ablation margin delineated by EDE and to determine whether the entire tumor with sufficient surrounding normal tissue has been treated. Comparison of EDE results with those of a clinical gold standard such as contrast-enhanced CT is therefore essential.

Acknowledgments—This study was funded by National Institutes of Health Grant 2 R01 CA112192. We are grateful to Siemens Medical Solutions USA, Inc., for providing the S2000 Axius Direct Ultrasound Research Interface (URI) and Software licenses.

REFERENCES

Bharat S, Fisher TG, Varghese T, Hall TJ, Jiang J, Madsen EL, Zagzebski JA, Lee FT Jr. Three-dimensional electrode displacement elastography using the Siemens C7 F2 FourSight four-dimensional ultrasound transducer. *Ultrasound Med Biol* 2008a;34:1307–1316.

Bharat S, Techavipoo U, Kiss MZ, Liu W, Varghese T. Monitoring stiffness changes in lesions after radiofrequency ablation at different temperatures and durations of ablation. *Ultrasound Med Biol* 2005;31:415–422.

Bharat S, Varghese T, Madsen EL, Zagzebski JA. Radio-frequency ablation electrode displacement elastography: A phantom study. *Med Phys* 2008b;35:2432–2442.

Bharat S, Varghese T. Radiofrequency electrode vibration-induced shear wave imaging for tissue modulus estimation: A simulation study. *J Acoust Soc Am* 2010;128:1582–1585.

Bing KF, Rouze NC, Palmeri ML, Rotemberg VM, Nightingale KR. Combined ultrasonic thermal ablation with interleaved ARFI image monitoring using a single diagnostic curvilinear array: A feasibility study. *Ultrason Imaging* 2011;33:217–232.

Chen H, Varghese T. Multilevel hybrid 2-D strain imaging algorithm for ultrasound sector/phased arrays. *Med Phys* 2009;36:2098–2106.

Chen L, Treece GM, Lindop JE, Gee AH, Prager RW. A quality-guided displacement tracking algorithm for ultrasonic elasticity imaging. *Med Image Anal* 2009;13:286–296.

Clevert DA, Paprottka PM, Helck A, Reiser M, Trumm CG. Image fusion in the management of thermal tumor ablation of the liver. *Clin Hemorheol Microcirc* 2012;52:205–216.

Deng Y, Palmeri ML, Rouze NC, Rosenzweig SJ, Abdelmalek MF, Nightingale KR. Analyzing the impact of increasing mechanical index and energy deposition on shear wave speed reconstruction in human liver. *Ultrasound Med Biol* 2015;41:1948–1957.

DeWall RJ, Bharat S, Varghese T, Hanson ME, Agni RM, Kliewer MA. Characterizing the compression-dependent viscoelastic properties of human hepatic pathologies using dynamic compression testing. *Phys Med Biol* 2012a;57:2273–2286.

DeWall RJ, Varghese T. Improving thermal ablation delineation with electrode vibration elastography using a bidirectional wave propagation assumption. *IEEE Trans Ultrason Ferroelectr Freq Control* 2012;59:168–173.

DeWall RJ, Varghese T, Brace CL. Visualizing *ex vivo* radiofrequency and microwave ablation zones using electrode vibration elastography. *Med Phys* 2012b;39:6692–6700.

Fahey BJ, Nelson RC, Hsu SJ, Bradway DP, Dumont DM, Trahey GE. In vivo guidance and assessment of liver radio-frequency ablation with acoustic radiation force elastography. *Ultrasound Med Biol* 2008;34:1590–1603.

Hall TJ, Zhu Y, Spalding CS. In vivo real-time freehand palpation imaging. *Ultrasound Med Biol* 2003;29:427–435.

Harari CM, Magagna M, Bedoya M, Lee FTJ, Lubner MG, Hinshaw JL, Ziemlewicz T, Brace CL. Microwave ablation: Comparison of simultaneous and sequential activation of multiple antennas in liver model systems. *Radiology* 2015;278:95–103.

Hoyt K, Castaneda B, Parker KJ. Two-dimensional sonoelastographic shear velocity imaging. *Ultrasound Med Biol* 2008;34:276–288.

Ingle A, Varghese T. Three-dimensional sheaf of ultrasound planes reconstruction (SOUPR) of ablated volumes. *IEEE Trans Med Imaging* 2014;33:1677–1688.

Jiang J, Brace C, Andreano A, DeWall RJ, Rubert N, Fisher TG, Varghese T, Lee F Jr, Hall TJ. Ultrasound-based relative elastic modulus imaging for visualizing thermal ablation zones in a porcine model. *Phys Med Biol* 2010;55:2281–2306.

Kiss MZ, Daniels MJ, Varghese T. Investigation of temperature-dependent viscoelastic properties of thermal lesions in *ex vivo* animal liver tissue. *J Biomech* 2009;42:959–966.

Kolokythas O, Gauthier T, Fernandez AT, Xie H, Timm BA, Cuevas C, Dighe MK, Mitsumori LM, Bruce MF, Herzka DA, Goswami GK, Andrews RT, Oas KM, Dubinsky TJ, Warren BH. Ultrasound-based elastography: A novel approach to assess radio frequency ablation of liver masses performed with expandable ablation probes: a feasibility study. *J Ultrasound Med* 2008;27:935–946.

Lencioni R, Crocetti L. Radiofrequency ablation of liver cancer. *Tech Vasc Interv Radiol* 2007;10:38–46.

Lencioni R, Crocetti L. Local-regional treatment of hepatocellular carcinoma. *Radiology* 2012;262:43–58.

Liang P, Wang Y. Microwave ablation of hepatocellular carcinoma. *Oncology* 2007;72(Suppl 1):124–131.

Lu MD, Xu HX, Xie XY, Yin XY, Chen JW, Kuang M, Xu ZF, Liu GJ, Zheng YL. Percutaneous microwave and radiofrequency ablation for hepatocellular carcinoma: A retrospective comparative study. *J Gastroenterol* 2005;40:1054–1060.

Lubner MG, Brace CL, Ziemlewicz TJ, Hinshaw JL, Lee FT Jr. Microwave ablation of hepatic malignancy. *Semin Interv Radiol* 2013;30:56–66.

- Malone DE, Lesiuk L, Brady AP, Wyman DR, Wilson BC. Hepatic interstitial laser photocoagulation: Demonstration and possible clinical importance of intravascular gas. *Radiology* 1994;193:233–237.
- Maluccio M, Covey A. Recent progress in understanding, diagnosing, and treating hepatocellular carcinoma. *CA Cancer J Clinicians* 2012;62:394–399.
- Mariani A, Kwiecinski W, Pernot M, Balvay D, Tanter M, Clement O, Cuenod CA, Zinzindohoue F. Real time shear waves elastography monitoring of thermal ablation: *In vivo* evaluation in pig livers. *J Surg Res* 2014;188:37–43.
- Minami Y, Kudo M. Review of dynamic contrast-enhanced ultrasound guidance in ablation therapy for hepatocellular carcinoma. *World J Gastroenterol* 2011;17:4952–4959.
- Murakami R, Yoshimatsu S, Yamashita Y, Matsukawa T, Takahashi M, Sagara K. Treatment of hepatocellular carcinoma: Value of percutaneous microwave coagulation. *AJR Am J Roentgenol* 1995;164:1159–1164.
- Nightingale KR, Palmeri ML, Nightingale RW, Trahey GE. On the feasibility of remote palpation using acoustic radiation force. *J Acoust Soc Am* 2001;110:625–634.
- Ophir J, Cespedes I, Ponnekanti H, Yazdi Y, Li X. Elastography: A quantitative method for imaging the elasticity of biological tissues. *Ultrasound Imaging* 1991;13:111–134.
- Potretzke TA, Ziemlewicz TJ, Hinshaw JL, Lubner MG, Wells SA, Brace CL, Agarwal P, Lee FTJ. Microwave versus radiofrequency ablation treatment for hepatocellular carcinoma: A comparison of efficacy at a single center. *J Vasc Interv Radiol* 2016;27:631–638.
- Qian GJ, Wang N, Shen Q, Sheng YH, Zhao JQ, Kuang M, Liu GJ, Wu MC. Efficacy of microwave versus radiofrequency ablation for treatment of small hepatocellular carcinoma: Experimental and clinical studies. *Eur Radiol* 2012;22:1983–1990.
- Righetti R, Kallel F, Stafford RJ, Price RE, Krouskop TA, Hazle JD, Ophir J. Elastographic characterization of HIFU-induced lesions in canine livers. *Ultrasound Med Biol* 1999;25:1099–1113.
- Rubert N, Bharat S, DeWall RJ, Andreano A, Brace C, Jiang J, Sampson L, Varghese T. Electrode displacement strain imaging of thermally-ablated liver tissue in an *in vivo* animal model. *Med Phys* 2010;37:1075–1082.
- Sarvazyan AP, Rudenko OV, Swanson SD, Fowlkes JB, Emelianov SY. Shear wave elasticity imaging: A new ultrasonic technology of medical diagnostics. *Ultrasound Med Biol* 1998;24:1419–1435.
- Shi H, Varghese T. Two-dimensional multi-level strain estimation for discontinuous tissue. *Phys Med Biol* 2007;52:389–401.
- Shibata T, Iimuro Y, Yamamoto Y, Maetani Y, Ametani F, Itoh K, Konishi J. Small hepatocellular carcinoma: Comparison of radiofrequency ablation and percutaneous microwave coagulation therapy. *Radiology* 2002;223:331–337.
- Shiina S, Tateishi R, Arano T, Uchino K, Enooku K, Nakagawa H, Asaoka Y, Sato T, Masuzaki R, Kondo Y, Goto T, Yoshida H, Omata M, Koike K. Radiofrequency ablation for hepatocellular carcinoma: 10-Year outcome and prognostic factors. *Am J Gastroenterol* 2012;107:569–577. quiz 578.
- Swan RZ, Sindram D, Martinie JB, Iannitti DA. Operative microwave ablation for hepatocellular carcinoma: Complications, recurrence, and long-term outcomes. *J Gastrointest Surg* 2013;17:719–729.
- Varghese T. Quasi-static ultrasound elastography. *Ultrasound Clin* 2009;4:323–338.
- Varghese T, Ophir J. An analysis of elastographic contrast-to-noise ratio. *Ultrasound Med Biol* 1998;24:915–924.
- Varghese T, Shi H. Elastographic imaging of thermal lesions in liver *in vivo* using diaphragmatic stimuli. *Ultrasound Imaging* 2004;26:18–28.
- Varghese T, Techavipoo U, Liu W, Zagzebski JA, Chen Q, Frank G, Lee FT Jr. Elastographic measurement of the area and volume of thermal lesions resulting from radiofrequency ablation: pathologic correlation. *AJR Am J Roentgenol* 2003a;181:701–707.
- Varghese T, Techavipoo U, Zagzebski JA, Lee FT Jr. Impact of gas bubbles generated during interstitial ablation on elastographic depiction of *in vitro* thermal lesions. *J Ultrasound Med* 2004;23:535–544. quiz 545–546.
- Varghese T, Zagzebski JA, Lee FT Jr. Elastographic imaging of thermal lesions in the liver *in vivo* following radiofrequency ablation: Preliminary results. *Ultrasound Med Biol* 2002;28:1467–1473.
- Varghese T, Zagzebski JA, Rahko P, Breburda CS. Ultrasonic imaging of myocardial strain using cardiac elastography. *Ultrasound Imaging* 2003b;25:1–16.
- Wells SA, Hinshaw JL, Lubner MG, Ziemlewicz TJ, Brace CL, Lee FT Jr. Liver ablation: Best practice. *Radiol Clin North Am* 2015;53:933–971.
- Xu H, Varghese T, Jiang J, Zagzebski JA. In vivo classification of breast masses using features derived from axial-strain and axial-shear images. *Ultrasound Imaging* 2012;34:222–236.
- Zhang M, Castaneda B, Christensen J, Saad WE, Bylund K, Hoyt K, Strang JG, Rubens DJ, Parker KJ. Real-time sonoelastography of hepatic thermal lesions in a swine model. *Med Phys* 2008;35:4132–4141.
- Zhao H, Song P, Urban MW, Kinnick RR, Yin M, Greenleaf JF, Chen S. Bias observed in time-of-flight shear wave speed measurements using radiation force of a focused ultrasound beam. *Ultrasound Med Biol* 2011;37:1884–1892.
- Zhou Z, Wu W, Wu S, Xia J, Wang CY, Yang C, Lin CC, Tsui PH. A survey of ultrasound elastography approaches to percutaneous ablation monitoring. *Proc Inst Mech Eng H* 2014;228:1069–1082.
- Ziemlewicz TJ, Hinshaw JL, Lubner MG, Brace CL, Alexander ML, Agarwal P, Lee FT Jr. Percutaneous microwave ablation of hepatocellular carcinoma with a gas-cooled system: Initial clinical results with 107 tumors. *J Vasc Interv Radiol* 2015;26:62–68.
- Ziemlewicz TJ, Wells SA, Lubner MG, Brace CL, Hinshaw JL, Lee FTJ. Hepatic tumor ablation. *Surg Clin North Am* 2016;96:315–339.